# Single particle thermometry in bimetallic plasmonic nanostuctures

Julian Gargiulo ( ✉ J.Gargiulo@physik.uni-muenchen.de )

Ludwig-Maximilians-Universität München   https://orcid.org/0000-0002-4524-3423

Matias Herran

Ludwig-Maximilians-Universitaet Muenchen

Ianina Violi

Instituto de Nanosistemas, Universidad Nacional de San Martín   https://orcid.org/0000-0001-8358-4336

Ana Sousa-Castillo

Ludwig-Maximilians-Universitaet Muenchen

Luciana Martinez

Centro de Investigaciones en Bionanociencias (CIBION), Consejo Nacional de Investigaciones Científicas y Técnicas (CONICET)   https://orcid.org/0000-0003-4860-2927

Simone Ezendam

Ludwig-Maximilians-Universität München

Mariano Barella

Centro de Investigaciones en Bionanociencias (CIBION), Consejo Nacional de Investigaciones Científicas y Técnicas (CONICET)

Helene Giesler

University of Duisburg-Essen

Roland Grzeschik

University of Duisburg-Essen

Sebastian Schluecker

University Duisburg Essen   https://orcid.org/0000-0003-4790-4616

Stefan Maier

Monash University   https://orcid.org/0000-0001-9704-7902

Fernando Stefani

National Scientific and Technical Research Council   https://orcid.org/0000-0002-3277-7215

Emiliano Cortes

Ludwig-Maximilians-Universität München

Article

Keywords:

# Abstract

Localized surface plasmons are lossy and generate heat. However, accurate measurement of the temperature of metallic nanoparticles under illumination remains an open challenge, creating difficulties in the interpretation of results across plasmonic applications. Particularly, there is a quest for understanding the role of temperature in plasmon-assisted catalysis. Bimetallic nanoparticles combining plasmonic with catalytic metals are raising increasing interest in artificial photosynthesis and the production of solar fuels. Here, we perform single-particle nanothermometry measurements to investigate the link between morphology and thermal performance of colloidal Au/Pd nanoparticles with two different configurations: Au core – Pd shell and Au core- Pd satellites. It is observed that the inclusion of Pd as a shell strongly reduces the photothermal response in comparison to the bare cores, while the inclusion of Pd as satellites keeps photothermal properties almost unaffected. These results contribute to a better understanding of energy conversion processes in plasmon-assisted catalysis.

# Introduction

Plasmonics metals are used in a broad range of applications due to their ability to efficiently confine and manipulate light into a subwavelength scale.[1,2] Most plasmonic materials are intrinsically lossy, meaning that their use is always accompanied by the generation of heat.[3,4] In the so-called field of thermoplasmonics, thermal effects have been exploited in a varied range of applications.[5,6] Despite this, quantitative and accurate experimental measurements of the generated nanoscale thermal fields remain a challenge, difficulting the understanding of the underlying mechanism in the experimental results.[7,8]

One area of research where reliable measurements of temperature are of special concern is plasmon-assisted catalysis.[9] Processes associated with plasmon excitation and decay can be beneficial for the chemical transformation of nearby molecules in a variety of ways.[10−12] These include charge carriers generation and injections, enhancement of the electromagnetic fields, resonant near-field energy transfers, and heating. All these phenomena can occur simultaneously under illumination, complicating the mechanistic understanding of energy flow during plasmon-assisted catalysis. In particular, understanding the role of heat is critical since the rates of chemical reactions usually present an exponential dependence on the temperature, as dictated by Arrhenius law.[13] Therefore, small temperature variations could lead to significant changes in the reaction rates. For this reason, significant efforts are being done to disentangle thermal and non-thermal effects in plasmon-assisted catalysis, [14−19] and the problem of reliable assessment of temperature has been identified as one of the bottlenecks for the development of the field.[20−22]. A deeper understanding and control of the mechanisms that accelerate reactions would be valuable to achieve superior efficiencies, milder reaction conditions (under solar irradiances and without bulk-scale heating or pressuring of the reactor),[23] or the manipulation of reaction pathways[24,25].

Despite the high potential of plasmon-assisted catalysis, traditional plasmonic metals are intrinsically poor catalysts for many reactions of interest. This has motivated the quest for new nanocomposites combining plasmonic metals with conventional catalytic metals (such as Pd, Pt, Rh, etc.).[26−28] The

inclusion of a second metal alters the frequency, quality factor, and decay pathways of the plasmon resonances. This allows the tuning of absorption to scattering ratio,[29] spatial distribution of reactivity,[30,31] and reaction selectivity.[32] In recent years, several morphological configurations of multimetallic plasmonic nanoparticles (NPs) have been tested, such as spherical core-shell (CS-NP), nanocubes,[33] partially coated NPs,[34] alloys,[35] core-satellites[36,37] and core-shell trimers[38], demonstrating promising results in artificial photosynthesis and the production of solar fuels.[39,40] However, the addition of new materials to a plasmonic NP also alters the processes of light absorption and heat conduction, in non-trivial ways depending on the overall material composition and its spatial distribution.[41–44] For example, the complexity of heat transport at surface facets and interfaces of hybrid NPs makes their photothermal modeling particularly challenging.[45] Here, this challenge is addressed experimentally, using hyperspectral Anti-Stokes (AS) thermometry.

AS thermometry exploits the fact that, upon illumination with a CW laser, the AS part of the photoluminescence (PL) spectrum of plasmonic NPs shows a temperature dependence.[46] This technique has been used for the thermal characterization of individual monometallic Au NPs such as disks, [47] pyramids,[48] rods,[49,50] bowties,[51] spheres[52,53] and cylinders.[54] Various implementations of AS thermometry have been reported, as reviewed by Baffou.[8] Recently, our group introduced a new implementation called hyperspectral AS thermometry, which retrieves the photothermal coefficient of individual NPs from a single PL hyperspectral image.[53] Unlike other optical methods for single particle thermometry of metals,[3] such as the ones based on fluorescence,[55] Raman,[56] DNA-PAINT,[57,58] optical rotation,[59] or refractive index variations,[60] hyperspectral AS thermometry is non-invasive, label-free and does not require any extra characterization or prior knowledge about the NPs or the medium properties.

Here, the optical and photothermal properties of bimetallic plasmonic NPs are studied. First, Au@Pd CS-NPs with different shell thicknesses are designed to investigate changes in their on-resonance photothermal response. It is shown that a Pd shell strongly reduces the heat generation in comparison with naked Au cores. The experimental studies are complemented with an analytical model for the photothermal response of CS-NPs. Second, the effect of the geometric configuration of bimetallic plasmonic NPs is assessed. Pd is shaped as either shell or satellites around the same Au nanospheres serving as core, keeping the plasmon frequency almost unaffected. It is found that the generation of heat is larger if the Pd is included as satellites around the Au core than if it is included as a shell, highlighting the role of the Au-Pd interfaces in the photothermal properties. These results shed light on the role of the catalytic material in the photon-phonon conversion processes of plasmonic-catalytic hybrids.

# Results

# Characterization and photothermal properties of Au-Pd Core Shell Nanoparticles:

Figure 1A illustrates the colloidal nanoparticles used in this first part of the study. They consist of Au nanospheres (Au NS) with a diameter of 67 nm, and Au@Pd core-shell nanoparticles (CS-NPs) with an Au core of 67 nm and Pd shells of ~ 2 and ~ 4 nm in thickness. The NPs were prepared using a seed-mediated growth strategy.[36] This method starts with the synthesis of small (seed) Au NS and the subsequent growth to the desired size, as described in the Materials and Methods sections. Two different shell thicknesses were obtained by varying the ratio of Au core and Pd salt. The three colloids are stabilized in water by means of cetyltrimethylammonium chloride (CTAC) capping. Figure 1B shows transmission electron microscopy (TEM) images of the obtained colloidal NPs. Au NSs are spherical, while the Au@Pd are more faceted. The spatial distribution of the two metals measured by Energy Dispersive X-Ray Spectroscopy (EDX) is presented as an inset in the bottom panel of Fig. 1B. While the signal of Au is confined to the core region, the Pd signal is uniformly distributed around the entire particle, as expected for a homogeneous coverage. Particle size histograms were obtained from TEM images and are shown in Fig. 1C. The median diameter of the Au NS is (66.6 ± 0.2) nm with a standard deviation of $\sigma$ =1.3 nm, while the two CS-NPs colloids have median sizes of (71.5 ± 0.1) nm with a standard deviation of $\sigma$=1.2 nm and (73.8 ± 0.2) nm with a standard deviation of $\sigma$ =1.7 nm. These values correspond to median Pd thicknesses of 2.4 ± 0.3 nm, and 3.6 ± 0.3 nm. For simplicity, we name them Au67 NS, Au67@Pd2 and Au67@Pd4. These parameters were employed to simulate the optical properties of the NP, as described in section S1 of the supplementary materials (SM). Figure 1D shows the numerically calculated absorption cross section spectra for different Pd thicknesses. The Pd shell leads to significant damping of the plasmon resonance of the Au core, reducing its amplitude and broadening its bandwidth. In addition, a small blue shift of the resonant frequency is predicted. In previous reports, a blue shift is observed for CS-NPs, [36] and a redshift for Au nanorods coated with Pd on the tips.[61] Fig. 1E shows the normalized experimental extinction spectra of the three synthesized colloids. The predicted broadening of the resonances due to the Pd shell is clearly observed. However, instead of a blue shift, the spectra exhibit slightly red-shifted resonances, which could also be attributed to the larger concentration of CTAC used as the stabilizing agent of the CS-NPs. [62]

In order to study optical and photothermal properties at the single particle level, arrays of well-separated individual NPs were fabricated on glass substrates using optical printing, as schematically shown in Fig. 2A.[63–65] Exemplary dark-field images of the optically printed grids are displayed in Fig. 2B. Having ordered arrays of isolated NPs facilitates the automation of data acquisition and allows the collection of larger datasets. It must be noted that the printing process does not alter the stability or composition of the NPs, as further discussed in section S2 of the SM. Figure 2C shows representative normalized scattering spectra for each type of NP. CS-NPs present a redshift and a broadening of their resonance with respect to the Au NS cores (see section S3 of the SM for further details). Because PL emission can provide insights into plasmon decay processes, it is relevant to investigate the emission properties of the NPs under study. Figure 2D shows PL spectra of the types of NPs, excited with CW laser excitation at 532 nm. This wavelength is suited to excite the plasmon resonance of three kinds of NPs. In agreement to reports on other NPs, we found that the shape of the PL spectra follows the characteristics of the scattering one. [66–69] Interestingly, the amplitude of the PL emission decreases with increasing Pd thicknesses. Qualitatively,

this decrease in PL emission is a result of the Pd damping the plasmon resonance of the Au core.[61] For quantitative analysis, the Stokes emission quantum yield $QY^S$ was calculated as the ratio between the total Stokes PL emission and the absorbed photons $QY^S_{PL} = \frac{\int_{543}^{\infty} PL(\lambda)d\lambda}{\sigma_{abs}(\lambda=532nm)I_{exc}}$, where $I_{exc}$ is the excitation irradiance (see section S4 of the SM for further details). In addition, the resonance quality is quantified as Q = $\frac{E_{res}}{\Gamma}$ where $E_{res}$ is the resonance energy and $\Gamma$ its full width at half maximum calculated from the scattering spectra. Figure 2E shows the measured $QY^S$ versus Q for the three NPs, showing a positive correlation. A similar trend was reported for Au nanorods and ascribed to enhanced emission due to an increased density of photonic states (Purcell effect). [61, 70−72]

After the optical characterization of the individual NPs, their photothermal response was measured using hyperspectral Anti Stokes (AS) thermometry with a CW 532 nm laser. The technique, as introduced by Barella $et.$ $al.$ [53], allows single particle photothermal characterization by raster scanning a laser over the NP, as schematized in Fig. 3A. In this way, heating and PL excitation are performed simultaneously with the same beam. Throughout the scanning, the relative position between the beam and the NP changes, leading to different excitation irradiances and hence, different steady state temperatures. In such a manner, a set of temperature-dependent PL emission spectra is collected. Figure 3B, shows three PL spectra for different irradiance levels for an illuminated Au67@Pd2 CS-NP. Processing the set of acquired PL spectra allows for finding the photothermal coefficient $\beta$, defined as

$$T^{NP} = \beta I_{exc} + T_0 \qquad (1)$$

where $T^{NP}$ and $T_0$ are the temperature of the particle in the presence and absence of light, respectively. For details on data processing, see section S5 of SM.

It must be noted that this method assumes that the PL emitting object has a homogeneous temperature $T^{NP}$. This condition is fulfilled by Au NS Under CW illumination,[3] and is also true for Au@Pd CS-NPs, as we demonstrate in the following. Figure 3D shows the calculated temperature increase $T(r) - T_0$ versus the radial coordinate $r$ for a Au67@Pd2 NP immersed in water under illumination at 532 nm with an irradiance of $I_{exc}$=1 mW/µm$^2$ (see Fig. 3C for the definition of the parameters and section S6 of SM for a full derivation of the calculus). The temperature is practically constant inside the CS-NP, except for a small drop $\nabla T_{Au-Pd}$ at the Au/Pd interface, shown in the inset of Fig. 3B. The temperature variations inside the CS-NP are $10^{-3}$ times smaller than the temperature increase of the NP surface. Hence, the NP can be described by a single, uniform temperature $T^{NP}$. This is a consequence of the high thermal conductivities of Au and Pd with respect to water, and the high electronic thermal conductance of the Au/Pd interface that allows efficient heat transfer through electron-electron scattering.[73] In addition, because Au and Pd have similarly high volumetric electron-phonon couplings, electrons and phonons equilibrate rapidly within each metal. For this reason, $T^{NP}$ refers indistinctly to the electronic or lattice temperature. (See Section

S7 for a quantitative comparison between lattice and electron gas temperatures). Thus, AS thermometry retrieves the photothermal coefficient of the entire CS-NPs.

Figure 3E shows histograms of the measured photothermal coefficients for the three systems under study. The median value obtained for the Au NS is $\beta_{Au67}$ is (51 ± 1) $\frac{K\mu m^2}{mW}$, in line with the one reported by Barella *et. al.* for 64 nm Au NS.[53] Interestingly, a significant reduction of $\beta$ is observed for the CS-NPs. The obtained median values of the Au67@Pd2 and Au67@Pd4 were $\beta_{Au67@Pd2}$ = (38 ± 1) $\frac{K\mu m^2}{mW}$ and $\beta_{Au67@Pd4}$ = (35 ± 1) $\frac{K\mu m^2}{mW}$, respectively. The standard deviation of the three measurements is $\sigma$ = 8 $\frac{K\mu m^2}{mW}$. Figure 3F (solid lines) shows the temperature increase versus excitation irradiance following Eq. 1, corresponding to the median $\beta$ of each type of NP. In dashed lines, the maximum irradiances used in each experiment are shown. The maximum temperature reached by the NPs was around 100°C. It must be noted that at these temperatures, the NPs are stable and no changes in their scattering or PL spectrum were observed during or after the measurements (see section S2 of the SM).

An analytical model was developed to calculate the temperature $T^{NP}$ of a NP surrounded by a media of thermal conductivity $\kappa_3$ and supported on a substrate with thermal conductivity $\kappa_4$. Details can be found in section Materials and Methods and sections S6-S8 of the SM. The temperature $T^{NP}$ is given by

$$T^{NP} = f\left(1 + \kappa_3 \frac{R_{2-3}^{th}}{a_3}\right)\frac{1}{4\pi\kappa_3 a_3}\sigma_{abs}I_{exc} + T_0 \qquad (2)$$

where $R_{2-3}^{th}$ is the Kapitza interfacial thermal resistances between the shell and the surrounding media, and $f = \left(1 - \frac{\kappa_4 - \kappa_3}{2(\kappa_4 + \kappa_3)}\right)$ is a factor that accounts for the role of the substrate in the heat dissipation. The solid black lines in Fig. 3E correspond to the photothermal coefficient $\beta$ predicted by Eq. (2) for Au@Pd CS-NPs as a function of the Pd shell thickness, for NPs on glass, surrounded by water and illuminated at 532 nm, as in the experiments. The calculation requires several thermodynamical constants for which accurate experimental values are scarce. This is the case for example for the Kapitza resistance between Pd and water $R_{Pd-Water}^{th}$. For this reason, we have included a maximum and a minimum calculated value, to represent the large dispersions of available data in the literature. A list of used parameters is shown in Table 2 in Section Materials and Methods. The calculations reasonably predict the experimental trends. However, it must be noted that for Au@Pd, half of the measured CS-NPs had a value below the predicted range. This could be due to several factors. i) An overestimation of the absorption cross sections: The simulations (shown in Fig. 1B and Figure S1) predict a 10 nm blue shift in the resonant frequency of CS-NPs, which is not observed experimentally. However, considering that the resonances are broad, a 10 nm detuning of the spectrum versus the excitation wavelength only modifies the absorption cross sections by less than 2% ii) The influence of the surfactant CTAC in the thermal resistance of the Pd-water interface.[74] iii) an overestimation of the factor $f$ accounting for the effect of the substrate in heat dissipation. For a spherical NP immersed in water on a glass substrate, $f$ takes a value of 0.875. However, Au@Pd CS-NPs are faceted, as shown in Fig. 1B, and can present a larger contact area with the substrate, enhancing heat

dissipation. Thermal simulations estimate a value of $f$ = 0.843 for faceted NPs, which is 4% smaller than its spherical counterpart (see section S12 of SM for details). To summarize, accurate theoretical predictions require a complete knowledge and modeling of every geometrical boundary, also including the liquid-substrate interface. Having a precise description of all these factors is challenging, making most predictions only approximate, and reinforcing the need for methods able to measure the temperature of nanoscale objects in their operation environments (i.e., *in situ*).

# Effect of morphology on photothermal properties of Au-Pd Nanosystems:

The functionalities of bimetallic nanostructures are not only determined by the material composition, but also by the spatial distribution of the constituents.[36] In the following, the effect of morphology on light-to-heat conversion for different Au-Pd bimetallic structures is investigated. Au NS 60 nm diameter cores were combined with Pd in two different configurations: i) assembled with 5 nm spherical Pd satellites NPs (named Au60-Pd-sat) and ii) coated with a homogeneous (1.8±0.3) nm Pd shell (named Au60@Pd2). Figure 4A shows an illustration of the three synthetized systems, as well as their corresponding TEM images. The average number of satellites per NP of the Au60-Pd-sat system was estimated from TEM images to be $\langle N_s \rangle = 160 \pm 30$. The approximated volume of Pd per Au core is $V_{Pd} = (1.0 \pm 0.2) \times 10^4 nm^3$ for Au60-Pd-sat and $V_{Pd} = (2.4 \pm 0.4) \times 10^4 nm^3$ for Au60@Pd2. This means that the amount of Pd is on the same order of magnitude for both configurations. Further characterizations of the NPs are presented in section S10 of the SM. Figure 4B shows the normalized extinction spectra of the three studied systems. Again, adding Pd to the Au cores results in plasmon damping and a decrease in the resonance quality, although larger damping was observed for the CS-NP. Arrays of single Au NS 60 nm and Au60@Pd2 CS-NPs were fabricated through optically printing on glass substrates. Instead, the Au60-Pd-sat were deposited by a drop-casting method, because the solution was not stable enough for the optical printing process. Figure 4C shows representative single particle PL emissions when excited with laser light at 532 nm in a water environment. The lower Q factor is reflected in a drop in the single particle PL emission. The decrease in PL emission is significantly larger in the Au60@Pd2 CS-NPs compared to the Au60-Pd-sat, indicating a larger plasmon damping. It must be noted that the Pd satellites interact weekly with light (see section S11 of SM) and absorb only a minor fraction of the incoming light (altogether less than 10%, when placed around the core).(35) Hence, the PL emission of the Au60-Pd-sat system is mostly emitted by the Au core.

Next, the photothermal coefficient of each system was determined using hyperspectral AS thermometry. The resulting histograms are presented in Fig. 4D. The median photothermal coefficient for the Au 60 NS cores was $\beta_{Au60}$ = (47 ± 1) $\frac{K\mu m^2}{mW}$ with a standard deviation of 8 $\frac{K\mu m^2}{mW}$. Remarkably, there's no significant difference with the median value for the core-satellites $\beta_{Au60-Pd-sat}$ = (46 ± 1) $\frac{K\mu m^2}{mW}$, with a larger standard deviation of 13 $\frac{K\mu m^2}{mW}$. If the PL is mostly emitted by the Au, the measured $\beta$ corresponds to the temperature of the core. By contrast, a significant reduction of the photothermal coefficient is observed for the CS-NPs, with a median of $\beta_{Au60@Pd2}$ = (29 ± 1) $\frac{K\mu m^2}{mW}$ and a standard deviation of 5 $\frac{K\mu m^2}{mW}$, in line with

the results presented in the previous section of this work. Overall, the experiments of this section point out that the presence of an interface between the two metals is crucial and dictates the photothermal response of the bimetallic nanostructures. The direct contact between Au and Pd enhances surface damping of the Au plasmon, leading to a poorer quality factor and lower absorption.

## Discussion

The optical and photothermal properties of individual bimetallic gold-palladium NPs in core-shell and core-satellite configurations were measured on glass substrates surrounded by water. Measured properties are summarized in Table 1. Photothermal coefficients were measured at an excitation wavelength of 532 nm, close to the NPs plasmon resonances of all systems. First, Au@Pd CS-NPs of 67 nm Au core and two different Pd thicknesses were studied. The inclusion of a Pd shell leads to poorer quality factors as evidenced by the broadening of scattering spectra and lower PL emission quantum yield. This is attributed to the enhanced surface damping of the plasmon in the Au-Pd interface and also causes a decrease in the absorption cross section. Using AS thermometry, it was found that the inclusion of a 2 nm thickness Pd shell leads to a reduction of the photothermal coefficient $\beta$ of 26% with respect to the bare Au core. However, the thickness of the Pd shell does not have a strong influence. Only a 6% decrease in the photothermal coefficient was observed when the Pd thickness was increased from 2.4 to 3.6 nm. Since Pd is highly conductive, it does not significantly restrict the conduction of heat, meaning that the absorption cross section of the Au-Pd CS-NPs is the main parameter influencing its photothermal coefficient. In addition, an analytical model was introduced for monometallic NS and bimetallic CS-NPs. Remarkably, this simple model predicts reasonably well the magnitude of the measured photothermal coefficients and their experimental trend. The model is applicable to other bimetallic CS-NPs systems (see section S12 of the SM for some examples). However, it slightly overestimates the value of $\beta$ for CS-NPs. A more accurate description would require precise information on interfacial thermal resistances, nanoscale boundaries, and the consideration of the liquid-substrate interaction. This level of description is challenging to achieve, highlighting the benefits of the experimental approach presented here.

Secondly, the influence of the Au-Pd interface in the photothermal properties was studied. It was found that coating the Au 60 nm cores with a 2 nm homogeneous shell of Pd reduces the photothermal coefficient by 38%, but that it remains practically unaffected when a similar amount of Pd is included in small satellites. A Pd shell introduces a stronger plasmon damping compared to the Pd satellites, as evidenced by the lower quality factor and weaker PL emission of the CS-NPs. This explains the lower absorption cross section and photothermal coefficient of CS-NPs. Overall, the experiments presented here highlight the importance of the interface for light to heat conversion.

Photothermal characterization at the single particle level enables a better understanding of the link between the NPs structure and the generated heat. As shown here, two systems with the same materials (in composition and quantity) can have very different thermal behaviors according to the spatial distributions of their constituents. In many cases, higher temperatures are desirable and beneficial in catalysis, despite other non-thermal mechanisms operating simultaneously. The type of studies presented

here provide guidelines for better exploitation of thermal fields. For example, it allows a more efficient deposition of the (typically scarce and expensive) catalytic materials on plasmonic systems, maximizing its photothermal effect. In addition, photothermal characterization can be combined with other studies of the role of morphology and composition in the reactivity of nanosystems[36, 75−77] to provide insightful information on energy transfer mechanisms and reaction pathways. In this regard, AS thermometry provides label-free, non-invasive, and *in situ* information at the single particle level, and therefore can potentially be employed under reaction conditions in the liquid or gas phase (as shown here by the measurements done in aqueous media). For this reason, it is envisioned that AS thermometry will be applied to many other complex/hybrid interfaces with catalytic relevance, such as metal-semiconductors or metal-organic materials.[40] More broadly, it is believed that AS thermometry can contribute to a better understanding of the role of temperature, not only in catalysis but also in the wide range of applications of hybrid or complex plasmonic materials.

Table 1
Summary of optical and photothermal properties of Au/Pd NPs.

| | Diameter (nm) | Extinction $\lambda_{max}$ (nm) | Scattering $\lambda_{max}$ (nm) | Scattering FWHM (nm) | $\dfrac{QY^{Stokes}}{QY_{Au67@Pd}}$ | Photothermal $\beta\left(\dfrac{K\mu m^i}{mW}\right)$ |
|---|---|---|---|---|---|---|
| AuNS-67nm | 66.6 | 535 | 551 ± 3 | 80 ± 3 | 2.8 | 51 ± 1 |
| Au67@Pd2 | 71.5 | 543 | 561 ± 2 | 119 ± 6 | 1.3 | 38 ± 1 |
| Au67@Pd4 | 73.8 | 543 | 565 ± 3 | 155 ± 16 | 1 | 35 ± 1 |
| AuNS-60nm | 59 | 532 | 547 ± 2 | 77 ± 3 | 2.3 | 47 ± 1 |
| Au60-Pd-sat | 59* (cores) | 535 | 547 ± 2 | 79 ± 3 | - | 46 ± 1 |
| Au60@Pd2 | 63 | 530 | 551 ± 2 | 106 ± 9 | 0.7 | 29 ± 1 |

# Materials And Methods

# Chemicals

Gold (III) chloride trihydrate ($HAuCl_4 \cdot 3H_2O$, ≥ 99.9%), ascorbic acid (AA, ≥ 99.0%), sodium borohydride ($NaBH_4$, ≥ 98%), cetyltrimethylammonium bromide (CTAB, ≥ 99.0%), cetyltrimethyl chloride (CTAC, 25 wt% in water), tetraethylorthosilicate 98% (TEOS), Polyvinylpyrrolidone (PVP, $M_W$:10.000) ,ammonium hydroxide solution ($NH_4OH$, 27 wt% in water) and absolute ethanol (EtOH) were all purchased from Sigma-Aldrich and used without further purification. In all experiments, ultrapure water with a resistivity of 18.2 MΩ cm was used.

# Synthesis of 60 and 67 nm Au NS

Au nanoparticles were prepared using a seed-mediated growth strategy described by Zheng *et. al.*[78] with some modifications to scale up the reaction. This protocol involves the synthesis of Au seed particles and the subsequent growth to the desired size, as described below:

Step1: Au Clusters

The initial Au seeds were formed by reducing 5 mL of an aqueous solution containing 0.25 mM $HAuCl_4$ and 0.1 M CTAB with 300 µL of a freshly prepared 10 mM $NaBH_4$ solution (ice-bath). The solution turns brownish within seconds indicating clusters formation. The clusters were kept undisturbed for 3 h at 27°C.

Step 2: 10 nm Au NS Synthesis

In a 20 mL glass vial, 4 mL of a 200 mM CTAC solution, and 3 mL of a 100 mM ascorbic acid (AA) solution were mixed, followed by the addition of 100 µL of previously prepared CTAB capped Au seeds. After the solution was stirred at 300 rpm and left at 27°C for 10 min, 4 mL of 0.5 mM $HAuCl_4$ were added in a quick one-shot injection. The resulting 10 nm Au spheres were centrifuged twice at 13400 rpm for 30 min and finally redispersed in 1 mL of a 20 mM CTAC solution.

Step 3: 60 and 67 nm Au NS Synthesis

200 mL of a 100 mM CTAC solution were mixed with 1.3 mL of a 100 mM AA solution and 225 or 250 µL of 10 nm Au NS solution in order to obtain 67 and 60 nm Au NS, respectively. The whole solution was kept stirred at 800 rpm at 27°C for 20 min. Then, 10 mL of 10 mM $HAuCl_4$ were pumped in at a rate of 20 mL $h^{-1}$ and once the pumping completed, was left stirring for 30 min. After two centrifugation-redispersion cycles (4000 rpm, 10 min) the Au NS were finally redispersed in 35 mL of ultrapure $H_2O$.

# Synthesis of Au@Pd CS-NPs

To grow a 2 nm Pd shell on top of the 60 and 67 nm Au Cores, we used a method that was described in the literature(*36*) Firstly, a solution containing 1.785 mL of a CTAC solution, 2.30 mL of a 0.2 M CTAB solution, 400 µL of a 10 mM $K_2PdCl_4$ and 13.96 mL of a ultrapure $H_2O$ were kept at 100°C for 60 min. Secondly, 1.753 mL of an aqueous solution containing $\approx 7.5 \times 10^{11}$ Au NS were added at 100°C, followed by the quick injection of 1 mL of 100 mM AA solution. The solutions immediately turned purple and were left at 100°C for another 60 min. Finally, two centrifugation-redispersion cycles (3000 rpm for 10 min) were carried out.

Alternatively, to grow a 4 nm Pd shell on 67 nm Au NS, the same procedure was followed, but using 1.753 mL of an aqueous solution containing $6.0 \times 10^{11}$ Au NS.

The Au67@Pd2 and Au67@Pd4 were redispersed in 20 mM CTAC, while Au67@Pd2 was redispersed in ultrapure $H_2O$.

# Synthesis of Au–Pd Core-Satellites NPs

Step 1. Synthesis of Palladium satellites

PVP-stabilized Pd nanoparticles (Pd NPs) were synthesized according to a method described in the literature with some modifications. (82) Briefly, 45 mL of aqueous solution containing 1.05 mM PVP and 4.25 mM of AA was heated up to 100°C under reflux for 10 min. Subsequently, 5.0 mL containing 10 mM of $Na_2PdCl_4$ was added in one shot. The reaction was allowed to continue at 100°C for 3 h to obtain Pd NPs.

Step 2. Assembly of Au-Pd Core- Satellite NPs

4 mL of EtOH were added to 2.77 mL of a $2.72\times10^{14}$ Au NS/L aqueous solution, followed by the addition of 350 μL of non-washed Pd satellites. After stirring the solution at 400 rpm for 30 min, it was washed in low-binding DNA Eppendorf tubes twice at 3000 rpm for 20 min. The method is fully described by Herran *et. al.* [36]

# Optical Printing:

NPs were optically printed onto glass substrates according to the process described in previous works.[79,80] Briefly, the NPs suspension is placed on top of a positive substrate functionalized with Poly-(diallyl-dimethylammoniumchlorid) PDDA (Sigma-Aldrich, MW $\sim 400.000-500.000$). The process is carried out in an open chamber, employing a 532 nm laser (Ventus, Laser Quantum) and a 60x water-immersion (Olympus) objective with a NA = 1. Printing irradiance was adjusted for each system to optimize the printing time and to avoid morphological changes during the optical printing process. Typically, 8 mW/μm² was used to print 60 nm and 67 nm Au NP. For the Au67@Pd CS-NPs, the irradiance was set to 6 mW/μm² and for the Au60@Pd it was 5.4 mW/μm².

# Dark field microscopy and spectroscopy:

Dark field images and single NP spectra were acquired by employing a high-intensity visible-NIR light source (Thorlabs, OSL2IR) which was scattered by the sample and focused on 60x water-immersion (Olympus) through a dark field condenser. A digital color camera (Canon EOS-500D) was used to obtain dark field images of the NPs supported on the glass substrate. Unpolarized scattering spectra of each NP were measured with a Shamrock 500i spectrometer (Andor) and an EMCCD camera (Andor Ixon EM + 885), in a spectral range between 450 and 850 nm (1 nm resolution).

# Hyperspectral Confocal PL images:

For confocal hyperspectral PL imaging, a continuous wave 532 nm laser was focused near its diffraction limit with a mean beam waist of 311 nm. Scanning was achieved with a closed-loop piezoelectric stage (PI). Each confocal image was obtained with 10x10 pixels on a range of 0.8 x 0.8 μm², with a high electron multiplying gain (usually 150) and an integration time of 2.5 s each pixel. The PL spectra were measured from 500 nm to 600 nm range, employing two 532 nm notch filters to filter the laser line. Hyperspectral confocal images of 67 nm NS, Au67@Pd2 CS-NPs and Au67@Pd4 CS-NPs were acquired using a

maximum irradiance of 2.1, 2.8, and 2.7 mW/µm² respectively. For 60 nm Au NS, 60nm core-satellites AuNP@Pd, and Au60@Pd2 CS-NPs, the irradiances were 2.0, 2.4, and 4.9 mW/µm², respectively.

# AS Hyperspectral thermometry:

The method was applied as described in Barella et. al.[53]

and further explained in section S5 of the SM. In short, a set of PL spectra corresponding to different excitation irradiances $I_i^{exc}$ is extracted from the hyperspectral images. Then, all possible ratios $Q_{i,j}^{AS}$ between AS PL emissions are calculated and fitted with Eq. 3.

$$Q_{i,j}^{AS}\left(\lambda\right) = \frac{I_i^{exc}}{I_j^{exc}} \frac{e^{\frac{E(\lambda)-E(\lambda_{\text{exc}})}{k_B\left[T_0+\beta_{i,j}I_j^{\text{exc}}\right]}} - 1}{e^{\frac{E(\lambda)-E(\lambda_{\text{exc}})}{k_B\left[T_0+\beta_{i,j}I_i^{\text{exc}}\right]}} - 1}$$

3

with the photothermal coefficient $\beta_{i,j}$ the only unknown parameter, $E\left(\lambda\right)$ the energy of the photon and $k_B$ the Boltzmann constant. Then, all obtained photothermal coefficients $\beta_{i,j}$ are averaged to obtain a single $\beta$ for the scanned NP.

# Temperature modelling of Core@Shell nanoparticles:

The temperature T versus de radial coordinate r of a core@shell NPs is

$$r < b$$

$$T\left(r\right) = \frac{-q_1}{6\kappa_1}r^2 + c_1$$

$$b < r < a$$

6

$$T\left(r\right) = \frac{-q_2}{6\kappa_2}r^2 + \frac{c_2}{r} + c_3$$

$$r > a$$

$$T\left(r\right) = \frac{Q}{4\pi\kappa_3 r} + T_0$$

A visual description of the parameters is presented in Fig. 3C. A full derivation of Eq. 6 is provided in Section S6 of the Supplementary Materials. $\kappa_1$, $q_1$ and $b$ are the thermal conductivity, heat power density and radius of the core, while $\kappa_2$, $q_2$ and $a$ corresponds to the outer radius of the core-shell NP. $T_0$ is the room temperature and $c_1$, $c_2$, $c_3$ are integration constants given by $c_2 = \frac{\kappa_3}{\kappa_2}\frac{Q}{4\pi\kappa_3} - \frac{q_2 a^3}{3\kappa_2}$,

$c_3 = \frac{\kappa_3 R_{2-3}^{th} c_4}{a^2} + \frac{c_4}{a} + \frac{q_2 a^2}{6\kappa_2} - \frac{c_2}{a} + T_0$, and $c_1 = \frac{1}{3} q_1 b R_{1-2}^{th} + c_3 + \frac{c_2}{b} + \frac{q_1 b^2}{6\kappa_1} - \frac{q_2 b^2}{6\kappa_2} \cdot R_{1-2}^{th}$, and $R_{2-3}^{th}$ are the Kapitza interfacial thermal resistances between materials and $Q = \sigma_{abs}(\lambda) I_{exc}$ is the total absorbed heat by the NP.

The temperature drop inside the Au volume is $\nabla T_{Au} = T(b) - T(0) = \frac{-q_1}{6\kappa_1} b^2$.

The temperature drop at the Au/Pd interface is $\nabla T_{Au-Pd} = T(b^-) - T(b^+) = \frac{1}{3} q_1 b R_{Au-Pd}^{th}$

The temperature drop in Pd is $\nabla T_{pd} = T(a) - T(b) = \frac{-q_2}{6\kappa_1}\left(b^2 - a^2\right) + c_2\left(\frac{1}{b} - \frac{1}{a}\right)$

From these expressions, it can be shown that $\frac{T(a^-)-T(0)}{T(a^+)-T_0} \leq 10^{-3}$, meaning that temperature variations inside the NP are negligible. In that case, the temperature inside the NP becomes

$$T^{NP} = T(a^+) + \frac{Q}{4\pi a^2} R_{2-3}^{th} = Q\left(\frac{1}{4\pi\kappa_3 a} + \frac{R_{2-3}^{th}}{4\pi a^2}\right) + T_0$$

7

The presence of a substrate with thermal conductivity $\kappa_4$ will affect heat dissipation around the NP. This effect can be modeled by multiplying Eq. 7 by a heat dissipation factor

calculated by the image method, as described in section S8.

Calculation shown in Fig. 3D was made using Eq. 6 and the following parameters: $\kappa_1 = 318\frac{W}{mK}$, $\kappa_2 = 71\frac{W}{mK}$, $\kappa_3 = 0.6\frac{W}{mK}$, $R_{2-3}^{th} = 3 \times 10^{-9}\frac{m^2 K}{W}$, $R_{1-2}^{th} = 0.03 \times 10^{-9}\frac{m^2 K}{W}$, $\sigma_{abs} = 1.49 \times 10^{-14} m^2$, b = 33.5 nm, a = 35.5 nm, $I_{exc} = 1\frac{mW}{\mu m^2}$, $Q = \sigma_{abs} I_{exc}$, $q_1 = 0.7\frac{Q}{\frac{4}{3}\pi b^3}$, $q_2 = 0.3\frac{Q}{\frac{4}{3}\pi(a^3 - b^3)}$.

Calculation shown in Fig. 3F was made using Eq. 2 with the following parameters: $\kappa_1 = 318\frac{W}{mK}$, $\kappa_2 = 71\frac{W}{mK}$ and the values from Table 2 for the maximum and minimum plots.

Table 2
Thermodynamic constants used in this work.

| Parameter | Min Value | Reference | Max Value | Reference |
|---|---|---|---|---|
| $R_{Au-water}^{th}$ | $4 \times 10^{-9} \frac{m^2 K}{W}$ | [74,81] | $15 \times 10^{-9} \frac{m^2 K}{W}$ | [82] |
| $R_{Pd-water}^{th}$ | $1.8 \times 10^{-9} \frac{m^2 K}{W}$ [83] | | $2.4 \times 10^{-9} \frac{m^2 K}{W}$ [84] | |
| $\kappa_3$ | $0.6 \frac{W}{mK}$ | T = 20°C [3] | $0.68 \frac{W}{mK}$ | T = 80°C [3] |
| $\kappa_4$ | $1 \frac{W}{mK}$ | Supplier datasheet | $1.2 \frac{W}{mK}$ | [3] |
| $\sigma_{abs}(\lambda = 532nm)$ | See Table S2 Supplementary Information | | | |
| a | b + Pd Thickness | | | |
| b | 63.6 nm | Figure 1b | 71 nm | Figure 1b |

# Declarations

## Acknowledgments

## Author contributions:

Idea and experiments design: JG, EC

Colloidal Synthesis: MH, ASC

Colloidal characterizations: MH, ASC, HG, RG

Optical and photothermal measurements: JG, ILV, LPM

Thermal modeling: JG, MB, SE

Data processing and analysis: JG, LPM, MB

Supervision and Funding: JG, ILV, SS, SAM, FDS, EC

Figures: MH, JG, SE, ILV, LPM, ASC, MB

Writing—original draft: JG

Writing—review & editing: All authors.

**Competing interests:**

Authors declare that they have no competing interests.

**Data and materials availability:**

Software for data processing can be found at https://github.com/marianobarella/nanothermometry.

# References

1. Maier, S. A. *Plasmonics: Fundamentals and Applications*. (Springer, 2007).

2. Amendola, V., Pilot, R., Frasconi, M., Maragò, O. M. & Iatì, M. A. Surface plasmon resonance in gold nanoparticles: a review. J. Phys. Condens. Matter **29**, 203002 (2017).

3. Baffou, G. *Thermoplasmonics: Heating metal nanoparticles using light. Thermoplasmonics: Heating Metal Nanoparticles Using Light* (Cambridge University Press, 2017).

4. Khurgin, J. B. How to deal with the loss in plasmonics and metamaterials. Nat. Nanotechnol. **10**, 2–6 (2015).

5. Baffou, G., Cichos, F. & Quidant, R. Applications and challenges of thermoplasmonics. Nat. Mater. **19**, (2020).

6. Liu, G., Xu, J., Chen, T. & Wang, K. Progress in thermoplasmonics for solar energy applications. Phys. Rep. **981**, 1–50 (2022).

7. Quintanilla, M. & Liz-Marzán, L. M. Guiding Rules for Selecting a Nanothermometer. Nano Today **19**, 126–145 (2018).

8. Baffou, G. Anti-Stokes Thermometry in Nanoplasmonics. ACS Nano vol. 15 5785–5792

9. Camargo, P. H. C. & Cortés, E. *Plasmonic Catalysis From Fundamentals to Applications*. (John Wiley & Sons, Ltd, 2021).

10. Linic, S., Aslam, U., Boerigter, C. & Morabito, M. Photochemical transformations on plasmonic metal nanoparticles. Nat. Mater. **14**, 567–576 (2015).

11. Gargiulo, J., Berté, R., Li, Y., Maier, S. A. & Cortés, E. From Optical to Chemical Hot Spots in Plasmonics. Acc. Chem. Res. 52, 2525–2535 (2019).

12. Martirez, J. M. P., Bao, J. L. & Carter, E. A. First-Principles Insights into Plasmon-Induced Catalysis. Annu. Rev. Phys. Chem. **72**, 99–119 (2021).

13. Levine, I. N. *Physical Chemistry*. (McGraw-Hill Education, 2009).

14. Zhou, L. *et al.* Quantifying hot carrier and thermal contributions in plasmonic photocatalysis. Science. **362**, 69–72 (2018).

15. Dubi, Y. & Sivan, Y. "Hot" electrons in metallic nanostructures—non-thermal carriers or heating? Light Sci. Appl. **8**, (2019).

16. Zhang, X. *et al.* Plasmon-Enhanced Catalysis: Distinguishing Thermal and Nonthermal Effects. Nano Lett. **18**, 1714–1723 (2018).

17. Kamarudheen, R., W. Castellanos, G., P. J. Kamp, L., J. H. Clercx, H. & Baldi, A. Quantifying Photothermal and Hot Charge Carrier Effects in Plasmon-Driven Nanoparticle Syntheses. ACS Nano **12**, 8447–8455 (2018).

18. Baffou, G., Bordacchini, I., Baldi, A. & Quidant, R. Simple experimental procedures to distinguish photothermal from hot-carrier processes in plasmonics. Light Sci. Appl. **9**, 108 (2020).

19. Kamarudheen, R., Aalbers, G. J. W., Hamans, R. F., Kamp, L. P. J. & Baldi, A. Distinguishing Among All Possible Activation Mechanisms of a Plasmon-Driven Chemical Reaction. ACS Energy Lett. **5**, 2605–2613 (2020).

20. Zhan, C., Moskovits, M. & Tian, Z. Q. Recent Progress and Prospects in Plasmon-Mediated Chemical Reaction. Matter **3**, 42–56 (2020).

21. Cortés, E. *et al.* Challenges in Plasmonic Catalysis. ACS Nano **14**, 16202–16219 (2020).

22. Mascaretti, L. *et al.* ll Commentary Challenges in temperature measurements in gas-phase photothermal catalysis Commentary. Joule 1–6 (2022)

23. Mukherjee, S. *et al.* Hot electrons do the impossible: Plasmon-induced dissociation of H 2 on Au. Nano Lett. **13**, 240–247 (2013).

24. Devasia, D., Das, A., Mohan, V. & Jain, P. K. Control of Chemical Reaction Pathways by Light–Matter Coupling. Annu. Rev. Phys. Chem. **72**, 423–443 (2021).

25. Zhan, C. *et al.* Plasmonic nanoreactors regulating selective oxidation by energetic electrons and nanoconfined thermal fields. Sci. Adv. **7**, eabf0962 (2022).

26. Swearer, D. F. *et al.* Heterometallic antenna-reactor complexes for photocatalysis. *Proc. Natl. Acad. Sci. U. S. A.* **113**, 8916–20 (2016).

27. Sytwu, K., Vadai, M. & Dionne, J. A. Bimetallic nanostructures: combining plasmonic and catalytic metals for photocatalysis. Adv. Phys. X **4**, 1619480 (2019).

28. Robatjazi, H. *et al.* Plasmon-driven carbon–fluorine (C(sp 3)–F) bond activation with mechanistic insights into hot-carrier-mediated pathways. Nat. Catal. **3**, 564–573 (2020).

29. Li, K. *et al.* Balancing Near-Field Enhancement, Absorption, and Scattering for Effective Antenna–Reactor Plasmonic Photocatalysis. Nano Lett. **17**, 3710–3717 (2017).

30. Aslam, U., Chavez, S. & Linic, S. Controlling energy flow in multimetallic nanostructures for plasmonic catalysis. Nat. Nanotechnol. **12**, 1000–1005 (2017).

31. Engelbrekt, C., Crampton, K. T., Fishman, D. A., Law, M. & Apkarian, V. A. Efficient Plasmon-Mediated Energy Funneling to the Surface of Au@Pt Core-Shell Nanocrystals. ACS Nano **14**, 5061–5074 (2020).

32. Quiroz, J. *et al.* Controlling Reaction Selectivity over Hybrid Plasmonic Nanocatalysts. Nano Lett. **18**, 7289–7297 (2018).

33. Xu, P., Lu, W., Zhang, J. & Zhang, L. Efficient Hydrolysis of Ammonia Borane for Hydrogen Evolution Catalyzed by Plasmonic Ag@Pd Core-Shell Nanocubes. ACS Sustain. Chem. Eng. **8**, 12366–12377 (2020).

34. Lou, Z., Fujitsuka, M. & Majima, T. Pt-Au Triangular Nanoprisms with Strong Dipole Plasmon Resonance for Hydrogen Generation Studied by Single-Particle Spectroscopy. ACS Nano **10**, 6299–6305 (2016).

35. Kang, N. *et al.* Visible-Light Acceleration of H2 Evolution from Aqueous Solutions of Inorganic Hydrides Catalyzed by Gold-Transition-Metal Nanoalloys. ACS Appl. Mater. Interfaces **12**, 53816–53826 (2020).

36. Herran, M. *et al.* Tailoring Plasmonic Bimetallic Nanocatalysts Toward Sunlight-Driven H2 Production. Adv. Funct. Mater. (2022).

37. Gao, W. *et al.* Electromagnetic induction effect induced high-efficiency hot charge generation and transfer in Pd-tipped Au nanorods to boost plasmon-enhanced formic acid dehydrogenation. Nano Energy **80**, 105543 (2021).

38. Lee, S. *et al.* Core-Shell Bimetallic Nanoparticle Trimers for Efficient Light-to-Chemical Energy Conversion. ACS Energy Lett. **5**, 3881–3890 (2020).

39. Verma, R., Belgamwar, R. & Polshettiwar, V. Plasmonic Photocatalysis for CO2Conversion to Chemicals and Fuels. ACS Mater. Lett. **3**, 574–598 (2021).

40. Ezendam, S. *et al.* Hybrid Plasmonic Nanomaterials for Hydrogen Generation and Carbon Dioxide Reduction. ACS Energy Lett. **7**, 778–815 (2022).

41. Jauffred, L., Samadi, A., Klingberg, H., Martin Bendix, P. & B. Oddershede, L. Plasmonic Heating of Nanostructures. Chem. Rev. **119**, 8087–8130 (2019).

42. Lim, D. K. *et al.* Enhanced photothermal effect of plasmonic nanoparticles coated with reduced graphene oxide. Nano Lett. **13**, 4075–4079 (2013).

43. Penelas, M. J. *et al.* Importance of the Structural and Physicochemical Properties of Silica Nanoshells in the Photothermal Effect of Silica-Coated Au Nanoparticles Suspensions. Langmuir **38**, 3876–3886 (2022).

44. Borah, R. & Verbruggen, S. W. Silver–Gold Bimetallic Alloy versus Core–Shell Nanoparticles: Implications for Plasmonic Enhancement and Photothermal Applications. J. Phys. Chem. C **124**, 12081–12094 (2020).

45. Setoura, K., Okada, Y., Werner, D. & Hashimoto, S. Observation of Nanoscale Cooling Effects by Substrates and the Surrounding Media for Single Gold Nanoparticles under CW-Laser Illumination.

ACS Nano **7**, 7874–7885 (2013).

46. He, Y. *et al.* Surface enhanced anti-Stokes one-photon luminescence from single gold nanorods. Nanoscale **7**, 577–582 (2015).

47. Xie, X. & Cahill, D. G. Thermometry of plasmonic nanostructures by anti-S tokes electronic Raman scattering. Appl. Phys. Lett. **109**, (2016).

48. Hugall, J. T. & Baumberg, J. J. Demonstrating Photoluminescence from Au is Electronic Inelastic Light Scattering of a Plasmonic Metal: The Origin of SERS Backgrounds. Nano Lett. **15**, 2600–2604 (2015).

49. Carattino, A., Caldarola, M. & Orrit, M. Gold Nanoparticles as Absolute Nanothermometers. Nano Lett. **18**, 874–880 (2018).

50. Cai, Y.-Y. *et al.* Anti-Stokes Emission from Hot Carriers in Gold Nanorods. Nano Lett. **19**, 1067–1073 (2019).

51. Jones, S., Andrén, D., Karpinski, P. & Käll, M. Photothermal Heating of Plasmonic Nanoantennas: Influence on Trapped Particle Dynamics and Colloid Distribution. ACS Photonics **5**, 2878–2887 (2018).

52. Pensa, E. *et al.* Spectral Screening of the Energy of Hot Holes over a Particle Plasmon Resonance. Nano Lett. **19**, 1867–1874.

53. Barella, M. *et al.* In situ photothermal response of single gold nanoparticles through hyperspectral imaging anti-stokes thermometry. ACS Nano **15**, 2458–2467 (2021).

54. Wu, S., Hogan, N. & Sheldon, M. Hot Electron Emission in Plasmonic Thermionic Converters. ACS Energy Lett. **4**, 2508–2513 (2019).

55. Carlson, M. T., Khan, A. & Richardson, H. H. Local temperature determination of optically excited nanoparticles and nanodots. Nano Lett. **11**, 1061–1069 (2011).

56. Fang, Z. *et al.* Evolution of light-induced vapor generation at a liquid-immersed metallic nanoparticle. Nano Lett. **13**, 1736–1742 (2013).

57. Nooteboom, S. W., Wang, Y., Dey, S. & Zijlstra, P. Real-Time Interfacial Nanothermometry Using DNA-PAINT Microscopy. Small **18**, 2201602 (2022).

58. Reinhardt, P. A. *et al.* Toward Quantitative Nanothermometry Using Single-Molecule Counting. J. Phys. Chem. B **125**, 12197–12205 (2021).

59. Hajizadeh, F. *et al.* Brownian fluctuations of an optically rotated nanorod. Optica **4**, 746 (2017).

60. Baffou, G. *et al.* Thermal imaging of nanostructures by quantitative optical phase analysis. ACS Nano **6**, 2452–2458 (2012).

61. Forcherio, G. T. *et al.* Single-Particle Insights into Plasmonic Hot Carrier Separation Augmenting Photoelectrochemical Ethanol Oxidation with Photocatalytically Synthesized Pd-Au Bimetallic Nanorods. ACS Nano (2022)

62. Movsesyan, A. *et al.* Influence of the CTAB surfactant layer on optical properties of single metallic nanospheres. J. Opt. Soc. Am. A **36**, C78–C84 (2019).

63. Urban, A. S., Lutich, A. a., Stefani, F. D. & Feldmann, J. Laser Printing Single Gold Nanoparticles. Nano Lett. **10**, 4794–4798 (2010).

64. Guffey, M. J. & Scherer, N. F. All-Optical Patterning of Au Nanoparticles on Surfaces Using Optical Traps. Nano Lett. **10**, 4032–4038 (2010).

65. Gargiulo, J., Cerrota, S., Cortés, E., Violi, I. L. & Stefani, F. D. Connecting Metallic Nanoparticles by Optical Printing. Nano Lett. **16**, 1224–1229 (2016).

66. Dulkeith, E. *et al.* Plasmon emission in photoexcited gold nanoparticles. Phys. Rev. B - Condens. Matter Mater. Phys. **70**, 1–4 (2004).

67. Wackenhut, F., Failla, A. V. & Meixner, A. J. Multicolor microscopy and spectroscopy reveals the physics of the one-photon luminescence in gold nanorods. J. Phys. Chem. C **117**, 17870–17877 (2013).

68. Yorulmaz, M., Khatua, S., Zijlstra, P., Gaiduk, A. & Orrit, M. Luminescence Quantum Yield of Single Gold Nanorods. Nano Lett. **12**, 4385–4391 (2012).

69. Fang, Y. *et al.* Plasmon emission quantum yield of single gold nanorods as a function of aspect ratio. ACS Nano **6**, 7177–7184 (2012).

70. Cai, Y.-Y., Tauzin, L. J., Ostovar, B., Lee, S. & Link, S. Light emission from plasmonic nanostructures. J. Chem. Phys. **155**, 060901 (2021).

71. Ostovar, B. *et al.* Increased intraband transitions in smaller gold nanorods enhance light emission. ACS Nano **14**, 15757–15765 (2020).

72. Cai, Y. Y. *et al.* Photoluminescence of Gold Nanorods: Purcell Effect Enhanced Emission from Hot Carriers. ACS Nano **12**, 976–985 (2018).

73. Ge, Z., Cahill, D. G. & Braun, P. V. Thermal conductance of hydrophilic and hydrophobic interfaces. Phys. Rev. Lett. **96**, 1–4 (2006).

74. Park, J. & Cahill, D. G. Plasmonic Sensing of Heat Transport at Solid-Liquid Interfaces. J. Phys. Chem. C **120**, 2814–2821 (2016).

75. Negrín-Montecelo, Y. *et al.* Photophysical Effects behind the Efficiency of Hot Electron Injection in Plasmon-Assisted Catalysis: The Joint Role of Morphology and Composition. ACS Energy Lett. **5**, 395–402 (2020).

76. Negrín-Montecelo, Y. *et al.* Synergistic Combination of Charge Carriers and Energy-Transfer Processes in Plasmonic Photocatalysis. ACS Appl. Mater. Interfaces **14**, 35734–35744 (2022).

77. Hartman, T., Geitenbeek, R. G., Whiting, G. T. & Weckhuysen, B. M. Operando monitoring of temperature and active species at the single catalyst particle level. Nat. Catal. **2**, 986–996 (2019).

78. Zheng, Y., Zhong, X., Li, Z. & Xia, Y. Successive, Seed-Mediated Growth for the Synthesis of Single-Crystal Gold Nanospheres with Uniform Diameters Controlled in the Range of 5–150 nm. Part. \& Part. Syst. Charact. **31**, 266–273 (2014).

79. Violi, I. L. *et al.* Challenges on optical printing of colloidal nanoparticles. J. Chem. Phys. **156**, (2022).

80. Gargiulo, J. *et al.* Accuracy and Mechanistic Details of Optical Printing of Single Au and Ag Nanoparticles. ACS Nano **11**, 9678–9688 (2017).

81. Hu, H. & Sun, Y. Effect of nanopatterns on Kapitza resistance at a water-gold interface during boiling: A molecular dynamics study. J. Appl. Phys. **112**, (2012).

82. Harikrishna, H., Ducker, W. A. & Huxtable, S. T. The influence of interface bonding on thermal transport through solid-liquid interfaces. Appl. Phys. Lett. **102**, (2013).

83. Jesus Gerardo Vera. Temperature and Heat Flux Dependence of Thermal Resistance of Water/Metal Nanoparticle Interfaces. (Rice University, 2014).

84. Li, S., Chen, Y., Zhao, J., Wang, C. & Wei, N. Atomic structure causing an obvious difference in thermal conductance at the Pd-H2O interface: A molecular dynamics simulation. Nanoscale **12**, 17870–17879 (2020).

85. Gundrum, B. C., Cahill, D. G. & Averback, R. S. Thermal conductance of metal-metal interfaces. Phys. Rev. B - Condens. Matter Mater. Phys. **72**, 1–5 (2005).

86. Galinon, C. *et al.* Pd/Ag and Pd/Au interface specific resistances and interfacial spin flipping. Appl. Phys. Lett. **86**, 1–3 (2005).

87. Block, A. *et al.* Tracking ultrafast hot-electron diffusion in space and time by ultrafast thermomodulation microscopy. Sci. Adv. **5**, eaav8965 (2019).

88. Lin, Z., Zhigilei, L. V. & Celli, V. Electron-phonon coupling and electron heat capacity of metals under conditions of strong electron-phonon nonequilibrium. Phys. Rev. B - Condens. Matter Mater. Phys. **77**, 1–17 (2008).

89. Medvedev, N. & Milov, I. Electron-phonon coupling in metals at high electronic temperatures. Phys. Rev. B **102**, 1–22 (2020).

90. Wang, L., Sagaguchi, T., Okuhata, T., Tsuboi, M. & Tamai, N. Electron and Phonon Dynamics in Hexagonal Pd Nanosheets and Ag/Pd/Ag Sandwich Nanoplates. ACS Nano **11**, 1180–1188 (2017).

91. Wang, W. & Cahill, D. G. Limits to thermal transport in nanoscale metal bilayers due to weak electron-phonon coupling in Au and Cu. Phys. Rev. Lett. **109**, 1–5 (2012).
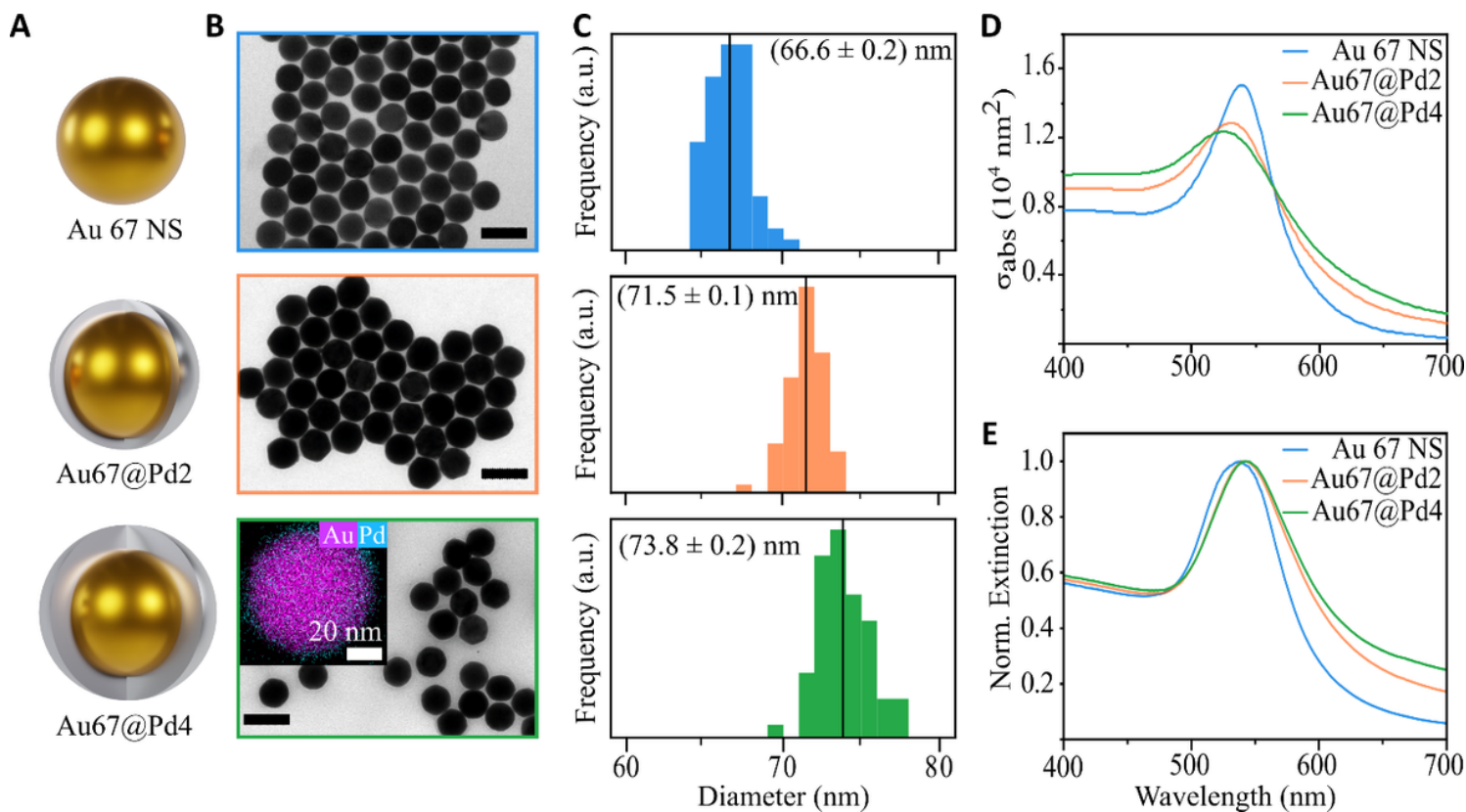
# Figures

**Figure 1**

**Synthesis and characterization of core-shell Au@Pd nanoparticles. A)** Visual illustration and **B)** TEM images of the three different studied NPs. Scale bars: 100 nm. The inset shows an EDX with the spatial distribution of the two metals. Au is shown in magenta and Pd in cyan. **C)** Size distributions. Medians are indicated with a black line and displayed in the labels. **D)** Calculated absorption cross sections in water. **E)** Experimental extinction spectra of the colloids. Each spectrum is normalized using its own maximum. In all figures, blue, orange and green correspond to Au67 NS, Au67@Pd2, and Au67@Pd4, respectively.
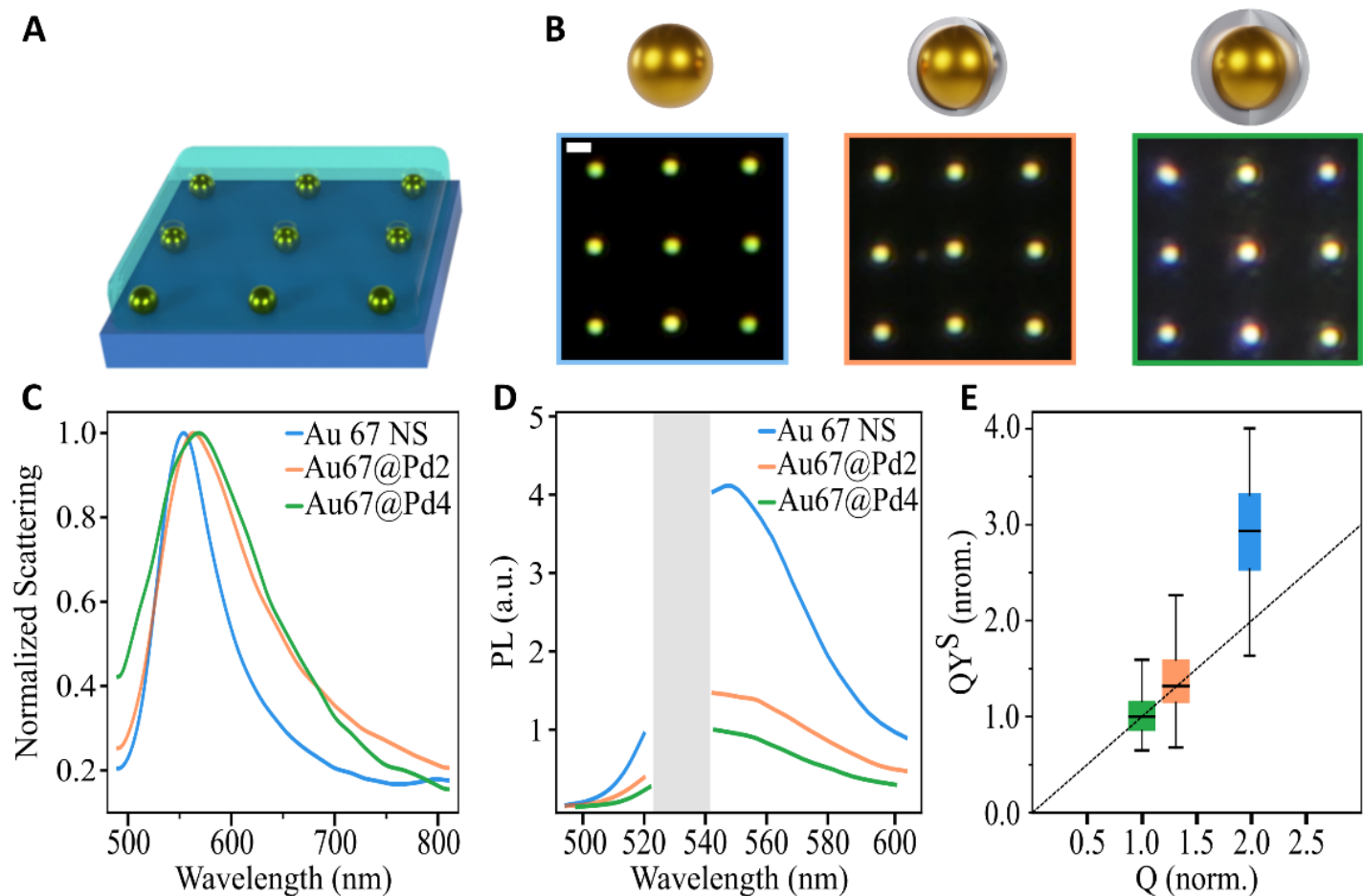
**Figure 2**

**Optical characterization of single Au@Pd core-shell nanoparticles. A)** Illustration of fabricated NPs grids on glass substrate immersed in water. **B)** Dark-field images of optically printed grids of individual NPs. Scale bar: 1 µm. **C)** Average of single particle scattering spectra, normalized to their maximum. **D)** Average of single particle PL emission spectra, excited with 1 mW/µm$^2$ of laser light at 532 nm. Grey band with no data corresponds to the laser rejection filter. **E)** Stokes PL emission quantum yield versus average Q-factor. Both magnitudes have been normalized by the measured value for the Au67@Pd4 system. In all figures, blue, orange and green correspond to Au67 NS, Au67@Pd2, and Au67@Pd4, respectively.
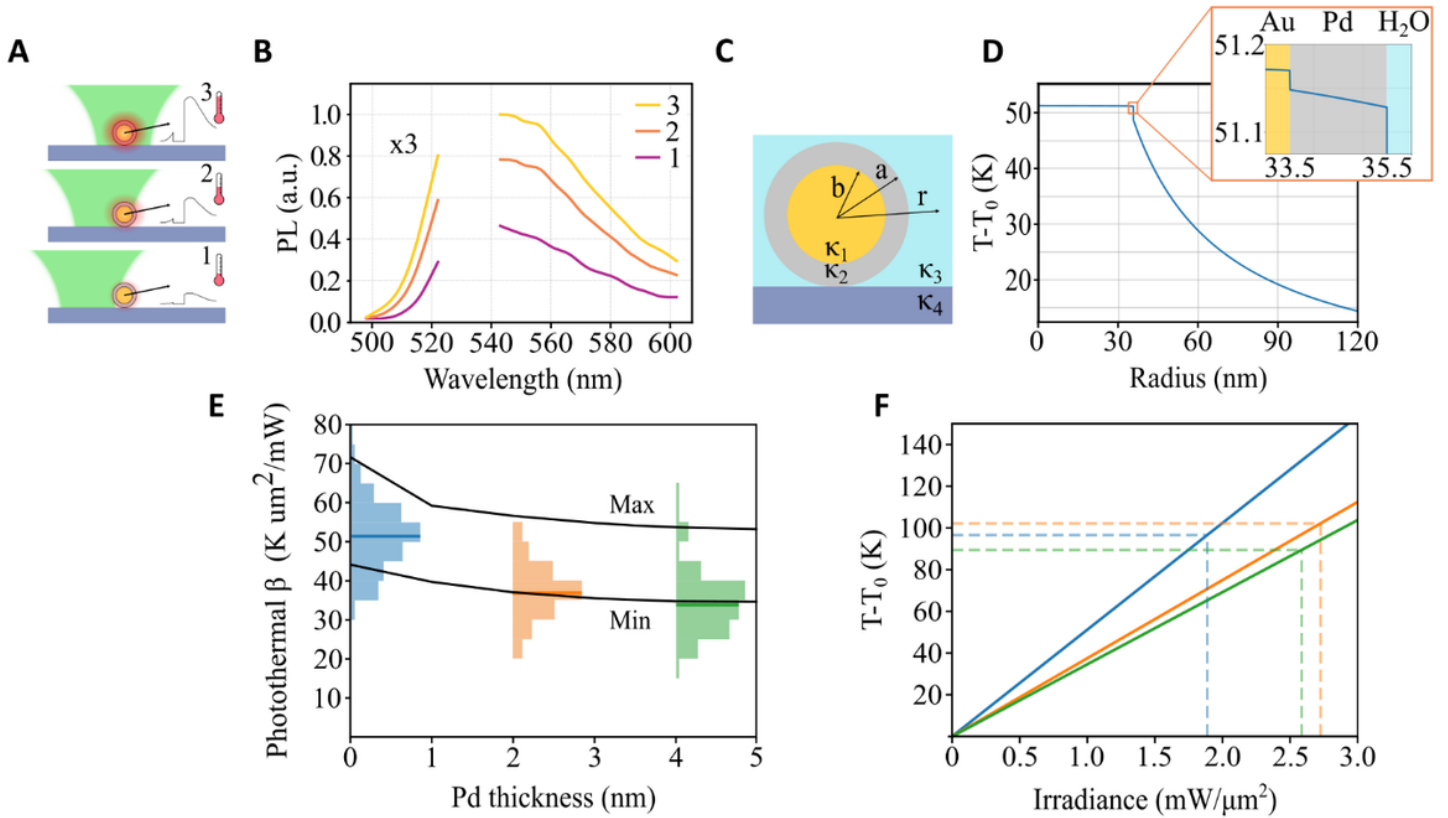
**Figure 3**

**Photothermal properties of single Au@Pd core-shell nanoparticles. A)** Illustration of the method for hyperspectral AS thermometry. **B)** Emission PL spectra of a single Au67@Pd2 NP at the following excitation irradiances. 1=1.27 mW/ μm², 2=2.19 mW/μm², 3= 2.78 mW/μm². The AS part has been multiplied by a factor of 3. Grey band with no data corresponds to the laser rejection filter. **C)** Illustration of the different constant used in Equation 2. **D)** Temperature versus radial coordinate for a Au67@Pd2 NP under an irradiance of =1 mW/μm². Details of the calculation are given in Materials and Methods. The inset shows a zoom on the region enclosed with an orange box, corresponding to the interface between the materials. **E)** Histograms of the experimental measured for the three systems under study. Blue: Au67 NS, Orange: Au67@Pd2, Green: Au67@Pd4. At least 85 different NPs were measured for each system, with a maximum of 250 NPs. Solid lines indicate the maximum and minimum theoretical calculation of photothermal coefficient versus thickness of the Pd shell using Equation 2. Parameters used in the calculus are listed in the Materials and Methods Section. **F)** Temperature increase versus irradiance for the three studied systems. Blue: Au67 NS, Orange: Au67@Pd2, Green: Au67@Pd4. The dashed lines correspond to the maximum irradiances used in the experiments. In all calculations and experiments presented in this figure, the NPs are immersed in water and irradiated at 532 nm.
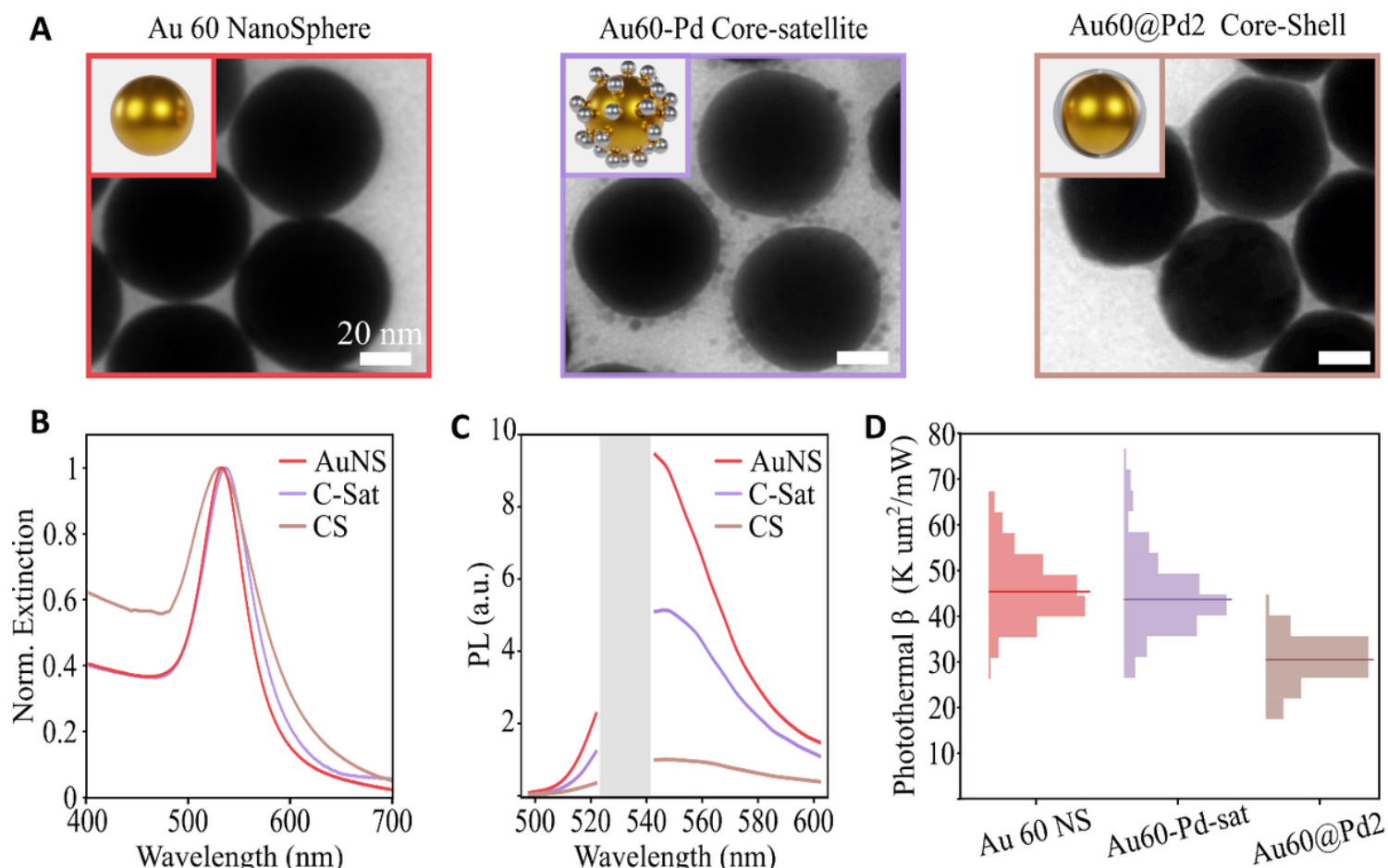
**Figure 4**

Optical and photothermal comparison between core-shell and core-satellites AuPd nanoparticles. A) Illustration and TEM images of the synthesized NPs. Scale bars: 20 nm. B) Experimental extinction spectra. Each spectrum is normalized using its own maximum. C) Average of single particle PL emission spectra of NPs on glass substrates and immersed in water, excited with 1 mW/μm$^2$ of laser light at 532 nm. Grey band with no data corresponds to the laser rejection filter. D) Histograms of the experimental measured photothermal coefficient for the three systems on glass substrates and immersed in water, at 532 nm.

## Supplementary Files

This is a list of supplementary files associated with this preprint. Click to download.

- GargiuloetalSi.docx